Строительные материалы и изделия
Construction Materials and Products

journal homepage: https://bstu-journals.ru

ISSN
2618-7183

**DOI: 10.58224/2618-7183-2026-9-5-3**

# Structure formation of a polychelate composite based on waste mining for hydro- and thermal insulation of tailings in the cryolithozone

**Pankov P.P.** [1], **Konovalova N.A.** * [1], **Bespolitov D.V.** [1], **Shavanov N.D.** [1], **Razmakhnin K.K.** [2], **Fediuk R.S.** [2]

[1] Transbaikal Institute of Railway Transport, Russia

**Abstract.** This paper presents a scientifically substantiated and experimentally validated study of the structure formation patterns of a polychelate composite based on a polymer matrix and enrichment waste used as a filler. It was established that cyclic cryogenic exposure ensures the formation of a heterogeneous, highly filled system with developed interphase zones. Using powder X-ray diffraction, basal reflections of layered hydrosilicates (muscovite-2M1 and kaolinite-2M) were recorded against a pronounced amorphous halo of the polymer matrix, demonstrating the chemisorption process without disrupting the crystalline structure of the filler. The observed polymorphic transformation of feldspars, with the transition of sanidine and microcline to orthoclase, indicates deep relaxation of internal microstresses in defective near-surface layers at the phase boundary. This process occurs due to the formation of coordination bonds between the functional groups of the matrix and the metal cations of the filler, which is confirmed by the high-frequency shift of the stretching vibrations of carboxylate anions in the infrared spectrum. The method of computed X-ray microtomography revealed the formation of a continuous spatial framework, the dominance of pores with sizes of 15-45 μm and the presence of a large number of isolated micropores with an average size of 13 μm. The spatial organomineral structure formed during cryogenic treatment is characterized by a low thermal conductivity coefficient (0.18 W/(m·K)) and the maximum water resistance grade (W20). The method of biotesting on test objects of two trophic levels proved the environmental safety of the developed material: the mortality rates of *Daphnia magna Straus* were 3.8–7.0%, deviations in the number of *Chlorella vulgaris Beijer* cells were 1.6-17.4%. The high efficiency of chemisorption immobilization of toxic components in the composite structure eliminates the risks of their desorption and leaching, which allows it to be recommended for reliable hydro- and thermal insulation of tailings storage facilities in cryolithozone conditions.

**Keywords:** gold mine tailings, permafrost degradation, seepage control barriers, polymer composites, cryostructuring, X-ray microtomography, immobilization of toxic components

*Corresponding author E-mail: roman44@yandex.ru

Received May 13, 2026; Received in revised form July 10, 2026; Accepted August 7, 2026

**Please cite this article as:** Pankov P.P., Konovalova N.A., Bespolitov D.V., Shavanov N.D., Razmakhnin K.K., Fediuk R.S. Structure formation of a polychelate composite based on waste mining for hydro- and thermal insulation of tailings in the cryolithozone. Construction Materials and Products. 2026. 9 (5). 3. DOI: 10.58224/2618-7183-2026-9-5-3

## 1. INTRODUCTION

In the technological cycles of gold extraction plants, as a result of deep enrichment of ore, millions of tons of highly dispersed waste are generated, which are sent to above-ground tailings storage facilities [1-5]. Moreover, the operation of tailings storage facilities in Arctic and subarctic regions is associated with geomechanical, hydrological and ecological risks of degradation of permafrost rocks in the base and body of enclosing dams due to the storage of warm pulp and high hydraulic loads [6-10]. One way to solve this problem is the installation of artificial anti-seepage and heat-insulating screens [11-14]. However, the effectiveness of their use in difficult climatic and geocryological conditions is limited by the technical shortcomings of traditional insulating materials. Clay screens are sensitive to cyclic freezing and thawing, as the temperature gradient promotes moisture migration, forming ice schlieren. Melting of these schlieren causes a network of macrocracks and increases the soil permeability. Rolled polymer geomembranes are subject to accelerated cryogenic aging and loss of elasticity at low temperatures, leading to mechanical failure under shear loads during subgrade thawing [15-20]. The remoteness of mining and processing plants from developed transportation infrastructure significantly reduces the economic viability of transporting significant volumes of high-quality raw materials for protective screens.

A promising solution to this problem is the development of frost-resistant waterproofing and thermal insulation composites based on locally available man-made raw materials—mining waste. Incorporating mining tailings into the production of composites with desired properties is consistent with the principles of a closed-loop economy and addresses a range of environmental issues [21-23]. Despite the classification of enrichment waste as extremely heaving systems, they have a developed specific surface area and a high reaction potential due to fine mechanical grinding of the ore. One of the ways to realize this potential is the formation of macromolecular coordination complexes at the interphase boundary of the heterogeneous "mineral filler - polymer matrix" system. The fundamental principles of cryostructuring of polymer systems filled with dispersed particles of various natures are presented in classical works [24-26], however, the process of targeted chemical bonding of components at the interphase boundary due to coordination effects has clearly not been sufficiently studied. In contrast to physical adsorption or mechanical encapsulation with the formation of chemically reversible adsorption contacts with low stability [27], coordination interaction promotes chemisorption fixation of functional groups of the polymer [28]. The effectiveness of targeted cryostructuring of highly filled dispersed systems of various origins for producing organomineral composite materials has been previously demonstrated by the authors in [29, 30].

The aim of this study is to investigate the cryostructuring mechanism of an organomineral composite with coordination-type interphase interactions and to scientifically substantiate its application in the construction of protective screens for tailings storage facilities.

Research objectives:

1. To scientifically substantiate the possibility of using gold ore deposit tailings as a dispersed filler for composite materials with specified properties based on an assessment of their reactivity potential.

2. To establish the physicochemical and rheological parameters of the polymer matrix, determining the homogeneity of the organomineral suspension and the spatial accessibility of its functional groups. 3. Study of the nature of interfacial physicochemical interactions and structural transformations of components in the contact zone at the matrix-filler interface.

4. Study of spatial topology parameters, determination of the volume fraction of the continuous framework and geometric characteristics of the composite pore space.

5. Determination of the physical, technical, and operational parameters of the developed material and a comprehensive assessment of its environmental safety to substantiate the possibility of its use in the design of protective screens for tailings storage facilities in the permafrost zone.

## 2. MATERIALS AND METHODS

### Experimental methods

The composite material is a structured organomineral hybrid system with a spatial framework organized through interfacial polychelation between the functional groups of the polymer matrix and the coordinatively unsaturated metal cations of the mineral filler. Beneficiation tailings (Zabaikalsky Krai, Russian Federation) with a high content of complexing metal cations were used as the dispersed filler of the matrix. The polymer matrix was obtained from aqueous solutions of a nonionic, water-soluble linear polyol and a high-molecular-weight carbon-chain polyelectrolyte bearing reactive carboxyl groups. The components were mixed in a 3:1 mass ratio at a total concentration of polymer components of 90 g/L, which ensured the dynamic viscosity level necessary for the sedimentation stability of the system. Homogenization of the polymer system was performed using an IKA C-MAG HS 10 magnetic stirrer at 500 rpm. To destroy intramolecular associates and ensure maximum segmental mobility of the polyol macromolecules, it was first dissolved under thermal action in the range of 90–95 °C until a clear solution was obtained. Subsequent mixing with the carbon-chain polyelectrolyte solution was performed with a controlled decrease in the reaction medium temperature. Optical monitoring of the structural integrity and homogeneity of the phases was performed using a Meiji Techno RZ ZOOM stereo microscope in transmitted light mode at a magnification of ×150. The physicochemical conditions of the studies and the parameters of the measuring equipment are presented in Table 1.

**Table 1.** Methods, instrumentation and physical and chemical conditions of research.

| Research methods /stages | Instrumentation and software | Technological parameters |
|---|---|---|
| Rotational viscometry / rheological properties of the polymer matrix | IKA Rotavisc hi-vi I Complete; Labworldsoft® 6 Visc | Temperature: 20 ± 2°C; Hydrodynamic mode: controlled shear rate variation; Measuring geometry: SP set-2 precision spindles; Maximum torque: 1.4374 mN·m |
| Turbidity spectrum method / supramolecular organization of the polymer matrix | Spectrophotometer KFK-3 | Optical path length: 30 mm; theoretical basis: Heller turbidity spectrum formalism; parameter to be determined: average radius of supramolecular structural elements |
| Gamma spectrometry/radiological characterization of the filler | Gamma spectrometer MKGB-01 "RADEK"; pulse analyzer MD-198; ASW | Energy range: 40–3000 keV; parameter being determined: specific effective activity of natural radionuclides ($^{226}$Ra, $^{232}$Th, $^{40}$K) |
| X-ray fluorescence analysis / chemical (oxide) composition of filler components | Bruker S4 Pioneer X-ray Fluorescence Spectrometer; SPEC-TRAplus | Emitter parameters: X-ray tube with a thin window (75 μm); high-voltage generator (up to 60 kV); maximum power: 4.5 kW |
| Powder X-ray diffraction / phase composition of filler components | X-ray diffractometer D8 Advance Bruker AXS; DIFFRACplus EVA (ICDD PDF-2 database) | Radiation: CuKα; imaging geometry: Bragg – Brentano; angle range 2θ = 3-60°; scanning step: 0.02°, exposure: 1 s/step; generator parameters: I = 40 mA, U = 40 kV; goniometer radius: 250 mm; Soller slits: 2.5 mm, Goebel mirror; scintillation counter; semi-quantitative phase analysis using the RIR method |
| FTIR spectroscopy / structural features and interfacial interactions | SHIMADZU FTIR-8400S Fourier Transform Infrared Spectrometer; IR-Solution | Configuration: based on a single-beam optical system with a Michelson interferometer; spectral range: 4000–400 cm$^{-1}$; quantitative spectral processing: baseline method |

Continuation of Table 1

| | | |
|---|---|---|
| Simultaneous thermal analysis (TG/DSC) / thermal stability and phase transformations | Synchronous thermal analyzer STA 449F1 NETZSCH; NETZSCH Proteus Analysis | Dynamic heating range: 30–1000°C; heating rate: 10°C/min; environment: dynamic argon (Ar) atmosphere; parameters to be determined: thermal stability, destruction kinetics, enthalpy of phase transformations and thermal processes |
| Scanning electron microscopy and energy dispersive spectroscopy / dispersion and elemental composition of the filler | Scanning electron microscope JSM-6510LV (JEOL); energy-dispersive spectrometer INCA Energy 350 (Oxford Instruments); sputtering unit JFC-1600 | Magnetron sputtering of platinum (Pt); parameters to be determined: dispersion, particle morphology, local elemental composition of mineral phases |
| High-resolution scanning electron microscopy / morphology and microstructure of the composite | Tescan Lyra 3 XMH scanning electron microscope; EDS Aztec X-Max 80 microanalysis system | Registration modes: secondary (SE) and reflected (BSE) electrons; sample preparation method: carbon layer deposition; coating parameters: thickness 10 nm; accelerating voltage: 15–20 kV |
| Computer X-ray microtomography / architecture and parameters of the pore space of the composite | SkyScan 1272 Bruker microCT X-ray microtomograph; NRecon 1.7.1.0, DataViewer 1.5.3.4, CTvox 3.3.0 r1403, CT Analyzer 1.16.9.0 + | Filter: 0.25 mm aluminum (Al); voltage: 60 kV; current: 180 μA; sample rotation: 0–180° in 0.2° steps; pixel size: 14–15 μm; frame format: 1224 × 820 pixels; exposure: 326 ms; the reconstruction interval based on the linear attenuation coefficient of radiation is normalized to optimize the contrast between the polymer and mineral phases. |
| Biotesting/assessment of acute toxic effects on a test object of the first trophic level | Spectrophotometer KFK-3; test object: algoculture *Chlorella vulgaris Beijer* | Methodology: PND F T 14.1:2:3:4.10-04 / T 16.1:2:2.3:3.7-04; analysis method: spectrophotometric control of optical density; exposure time 22 h; temperature: 36.0 ± 0.5°C; pH range 7.0-8.5 |
| Biotesting/assessment of acute toxic effects on a test object of the second trophic level | Climatostat; test object: crustacean *Daphnia magna Straus* | Methodology: FR.1.39.2007.03222; extract dilution factor: 1, 10, 100, 1000, 10000; exposure time: 96 h; temperature: 22.0°C; pH range 7.0-8.5 |

The composite material was produced by introducing a filler into a polymer matrix. The resulting organomineral suspension was placed in molds and held on a vibration stand for 2 minutes at 2800 rpm and an amplitude of 0.15 mm to remove entrained air and maintain the sedimentation stability of the heavy mineral phases. The resulting system was subjected to three cryogenic treatments to stabilize the composite's spatial framework. Cryostructuring consisted of freezing the suspension at -18±2°C, isothermal holding within this temperature range for 6 hours, and subsequent controlled thawing at 22±2°C.

The composite material's barrier efficiency and thermal insulation properties, which determine its performance under challenging climatic and geocryological conditions, were assessed after the final thawing of the samples. Thermal conductivity was measured using a probe method with a MIT-1 thermal conductivity meter in accordance with Russian Standard GOST 30256-94. Tight adhesion of the material to the probe was ensured by the elastic recovery forces of the polymer matrix. Water impermeability was assessed on samples pre-dried at room temperature using the accelerated air permeability resistance determination method in accordance with Russian Standard GOST 12730.5-2018. Air permeability measurements of surface layers were performed using a BB-2 vacuum device with a flange clamping force of 400 N, a pressure of 0.1 MPa, and an operating vacuum level of 0.070-0.075 MPa in the vacuum chamber.

To study surface homogeneity and record the infrared spectra of the original and filled polymer systems, thin films were cast and subjected to three cryogenic treatments. The resulting films were

dried at a temperature of 25±2°C for 24 hours to a constant weight to ensure the technical feasibility of recording spectra.

**Beneficiation tailings (BT).** Basic properties: beige dispersed material; bulk density – 1163.5 kg/m$^3$; true density – 2670.0 kg/m$^3$; specific surface area – 275.2 m$^2$/kg. The granulometric composition of GT is characterized by the following total residues on sieves of sizes 1.25; 0.90; 0.63; 0.315; 0.16; 0.14; 0.08 and 0.071 mm: 18.61 wt. %; 22.47 wt. %; 24.30 wt. %; 26.27 wt. %; 29.79 wt. %; 34.35 wt. %; 62.71 wt. %; 80.98 wt. %. The features of the grain composition allow classifying GT as a highly dispersed material. The small particle size combined with a large specific surface area can facilitate the creation of a significant interfacial contact area and intensify polychelation processes at the polymer matrix–filler interface. The particle distribution exhibits a pronounced pseudo-bimodal pattern: in addition to an ultrafine phase with an average particle size of 8.2 μm, there are fractions larger than 1.25 mm (18.61 wt.%), which represent loose macroaggregates (Fig. 1). The presence of easily degradable aggregates in the filler can ensure a denser spatial packing of BT within the polymer matrix.

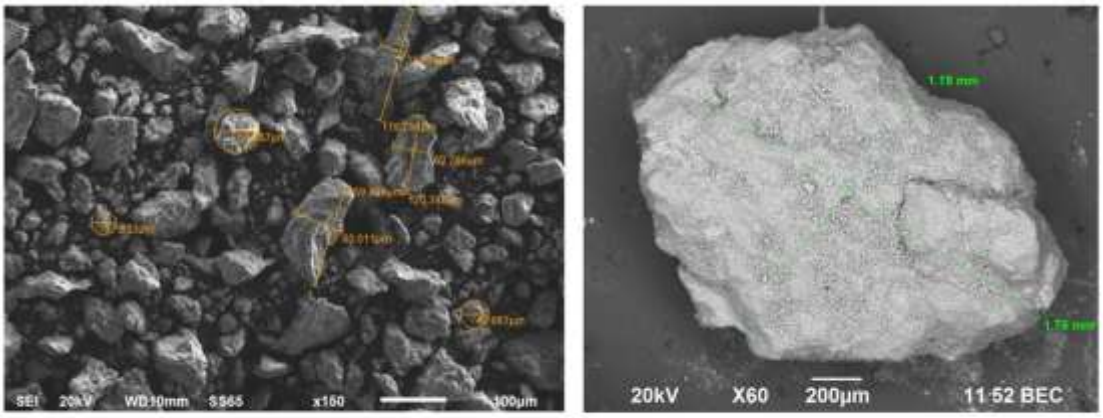


a b

**Fig. 1.** SEM images of beneficiation tailings: a – general particle morphology (SEI, ×150); b – rock macroaggregate (BEC, ×60).

Primary microparticles are characterized by an acute-angled morphology (Fig. 1a). The developed relief of the cleavages may indicate high surface energy and an excess of unsaturated chemical bonds formed during intensive destructive grinding of the ore, which is thermodynamically favorable for the subsequent chemisorption of functional groups in the polymer matrix. SEM image of the rock macroaggregate (Fig. 1b), obtained in backscattered electron mode, indicates pronounced phase heterogeneity, significant porosity, and cluster architecture of the material. The developed morphology can ensure high capillary activity and penetration of matrix macromolecular chains into the pore space of the BT. Subsequent formation of polychelate on the outer contour and in the internal volume of the pores can lead to the creation of a branched spatial network of interfacial entanglements between the filler and the matrix.

Chemical composition, wt. %: 67.23 $SiO_2$; 15.30 $Al_2O_3$; 4.33 $K_2O$; 4.10 $Na_2O$; 2.45 $Fe_2O_3$; 1.97 CaO; 0.84 MgO; 0.37 $TiO_2$; 0.13 $P_2O_5$; 0.03 MnO; 2.46 – loss on ignition.

X-ray diffraction analysis data indicate (Fig. 2a) that the composition of BT includes: quartz ($SiO_2$; d = 4.31 Å; 3.34 Å; 1.93 Å); dolomite ($CaMg(CO_3)_2$; d = 2.89 Å; 2.19 Å; 1.78 Å); anor-tite ($CaAl_2Si_2O_8$; d = 4.04 Å; 3.20 Å; 3.18 Å); albite ($NaAlSi_3O_8$; d = 4.01 Å; 3.67 Å; 3.23 Å); muscovite ($KAl_2[AlSi_3O_{10}](OH)_2$; d = 5.02 Å; 3.00 Å; 2.57 Å); sanidine ($K(AlSi_3O_8)$; d = 4.24 Å; 3.31 Å; 3.27 Å); wollastonite ($CaSiO_3$; d = 3.30 Å; 2.96 Å; 1.86 Å); kaolinite ($Al_2Si_2O_5(OH)_4$; d = 7.17 Å; 3.58 Å; 2.34 Å); microcline ($KAlSi_3O_8$; d = 6.47 Å; 3.71 Å; 2.57 Å). Data of semi-quantitative analysis of phase composition, wt. %: 27.62 albite; 24.99 quartz; 15.77 sanidine; 12.76 anorthite; 10.47 microcline; 2.57 dolomite; 2.43 wollastonite; 1.96 muscovite; 1.44 kaolinite.

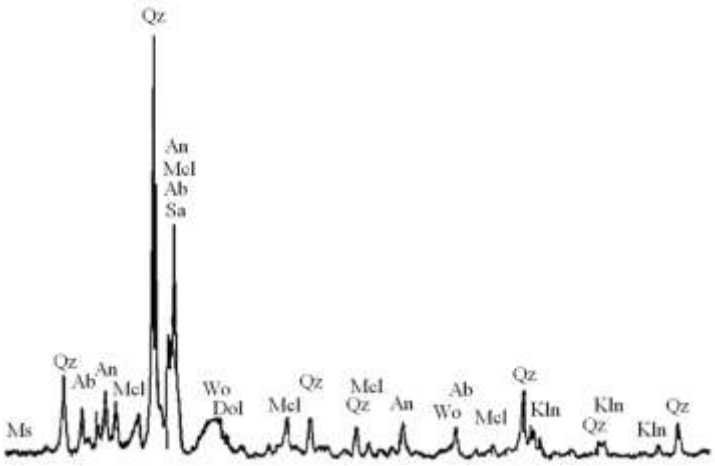


a

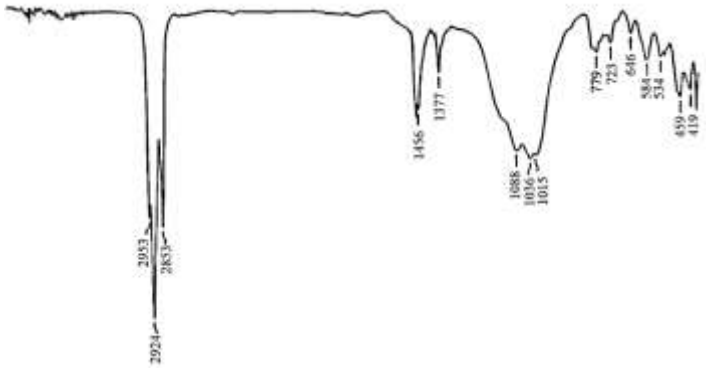


b

**Fig. 2.** X-ray diffraction pattern (a) and IR-spectra (b) of the beneficiation tailings: Ab – albite; Qz – quartz; An – anorthite; Mcl – microcline; Dol – dolomite; Kln – kaolinite; Wo – wollastonite; Ms – muscovite; Sa – sanidine.

Despite the numerical predominance of feldspar minerals, the diffraction pattern shows the dominance of the main analytical reflection of quartz (d = 3.34 Å). In the region of small and medium angles, an increase in background intensity and local broadening of the bases of the diffraction maxima are observed, which may indicate partial mechanochemical amorphization of the surface layers of minerals and the accumulation of crystal lattice defects as a result of intensive technological grinding of the ore. The selectivity of the destruction and amorphization processes is due to the high rigidity of the quartz crystalline framework, which manifests itself against the background of an intense transition to a disordered state of the near-surface layers of layered silicates (kaolinite, muscovite) and dolomite. The reactivity of BT is also associated with the high defectiveness of the structures of feldspar minerals (albite, anorthite, sanidine), caused by their isomorphic capacity. Defects and isomorphic substitutions in their structure can facilitate the release of coordinatively unsaturated metal cations into the highly defective cleavage surfaces, creating energetically favorable conditions for subsequent polychelation with functional groups of the matrix.

Muscovite and kaolinite (total content 3.4 wt%) are capable of initiating interfacial interaction processes. The surface hydroxyl groups ≡Al–OH and ≡Si–OH of these mineral phases, combined with iron oxide (2.45 wt%) and a metastable X-ray amorphous component, can form a system of active sites on the BT surface. These surface defects exhibit increased chemical activity and are capable of implementing donor-acceptor and coordination interactions with functional groups of the polymer matrix during the formation of a polychelate at the phase boundary. The structural features of BT were further investigated using infrared spectroscopy (Fig. 2b). The spectra were recorded as a powder suspension in vaseline oil. Consequently, intense absorption bands in the regions of 2953, 2924, and

2853 cm-1, related to the stretching vibrations of C–H bonds, as well as local peaks at 1456 and 1377 $cm^{-1}$, corresponding to deformation vibrations, were attributed to the hydrocarbon component of the immersion medium. The intrinsic spectral profile of GT in the region below 1200 $cm^{-1}$ is due to its silicate and aluminosilicate components, which is consistent with the X-ray diffraction analysis data. The most intense absorption band with differentiated maxima at 1088, 1036, and 1015 $cm^{-1}$ corresponds to asymmetric stretching vibrations of the Si–O–Si and Si–O–Al bonds in the crystal lattice of quartz and framework aluminosilicates (feldspars). The high degree of crystallinity of the silicon oxide phase is indicated by the presence of a characteristic doublet at 779 and 723 $cm^{-1}$ (Si–O deformation vibrations). Absorption bands with maxima at 646, 584, and 534 $cm^{-1}$ are associated with stretching and deformation vibrations of intralayer Si–O–Al and Al–O bonds in the octahedral layers of muscovite and kaolinite. Deformation vibrations of the O–Si–O bonds of the silicate framework are recorded in the low-frequency region at 459 and 419 $cm^{-1}$. Simultaneous thermal analysis (Fig. 3) revealed that the sample mass loss upon heating to 1000 °C was 1.96 wt.%. The low-temperature region is characterized by a minor mass loss of 0.10 wt.%, caused by the desorption of residual hygroscopic moisture. The exothermic effect at 487.7°C (specific energy 9.555 J/g) is accompanied by a mass loss of 0.12 wt.%, which is likely due to the oxidation of sulfide inclusions and trace impurities of flotation reagents, typical of gold deposit beneficiation waste.

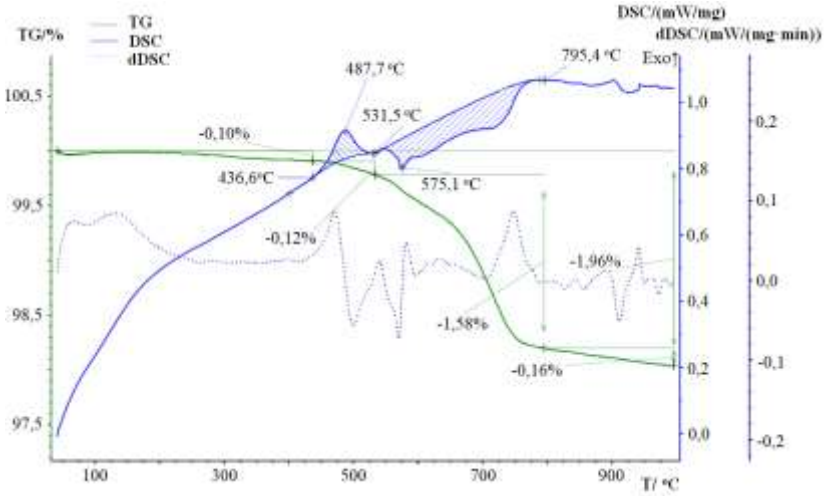


**Fig. 3.** TG, DSC, and DTG patterns of the beneficiation tailings.

An intense endothermic peak at 575.1°C indicates the presence of a highly crystalline $SiO_2$ structure. The TG curve shows no changes in this region, indicating a polymorphic transition from α-quartz to β-quartz caused by the rearrangement of the trigonal crystal lattice into a hexagonal modification. The significant intensity of this endothermic peak is consistent with the high content of the quartz phase according to X-ray diffraction analysis (24.99 wt.%) and the dominance of silicon dioxide in the bulk chemical composition (67.23 wt.%). The most intense stage of destruction (loss of 1.58 wt.%), caused by the decarbonization of mineral phases, is recorded in the range of 575.1–795.4°C. The endothermic effect with an enthalpy of -48.19 J/g is due to the intense dissociation of the carbonate component of dolomite according to the scheme:

$$CaMg(CO_3)_2 \rightarrow CaO + MgO + 2CO_2 \uparrow$$

The residual mass change at temperatures above 795.4°C is no more than 0.16 wt.%, indicating complete completion of the gas evolution processes. The total mass loss upon heating to 1000°C was 1.96 wt.%. Minor fluctuations in the DSC curve in the temperature range of 850-1000°C are recorded without mass change and correspond to solid-phase sintering of the inert silicate framework (albite, sanidine, microcline, anorthite), as well as structural rearrangement of the X-ray amorphous phase, previously recorded by powder diffraction. This predetermines the thermodynamic stability of GT

during its subsequent use as a filler in a polymer matrix. The DSC curve in the high-temperature region shows no pronounced thermal effects, which is also consistent with the X-ray diffraction analysis data on the predominance of the crystalline component in GT. Polymer matrix. Basic properties: density 1.18 g/cm3; viscosity 350 mPa s; pH = 6. The dynamic viscosity value measured before cyclic cryostructuring ensures optimal conditions for homogeneous distribution of matrix macromolecules in the interparticle (interstitial) space of GT. The established pH = 6 indicates partial ionization of the carboxyl groups of the polyelectrolyte macrochains. This promotes their conformational unfolding due to electrostatic repulsion forces and ensures high spatial accessibility of the functional groups for subsequent polychelation. The surface of the polymer matrix film, studied by stereomicroscopy, is characterized by high morphological homogeneity and the absence of visible shrinkage defects. This indirectly indicates the formation of an inversion morphological type with a uniform distribution of polyelectrolyte microdomains in the continuous phase of the linear polyol. This heterophase matrix organization can facilitate reliable adhesive contact with BT.

The mass-average radius of supramolecular formations, determined by turbidity spectra, was approximately 599 nm, indicating the formation of a size-stable secondary structure of the polymer matrix. This structure intensifies subsequent coordination interactions with the highly defective BT cleavage surfaces during their alignment.

The thermal transformations of the cryostructured matrix (Fig. 4) are characterized by multistage degradation, which is typical for interpolymer complexes with a system of cooperative hydrogen bonds. The thermogram reveals three main stages of thermal decomposition. The first stage occurs in the low-temperature region up to 180°C with an insignificant mass loss (0.10 wt%), which is caused by the removal of weakly bound hygroscopic moisture and the destruction of labile intermolecular contacts formed during cryogenic exposure.

The second stage is recorded in the temperature range of 200-370°C. Endothermic peaks form a multiplet profile with peaks at 223.7; 292.2, and 337.7°C. The endothermic effect at 223.7°C, which occurs virtually without mass loss, is associated with the melting of ordered crystalline domains of the linear polyol formed during cryogenic structuring of the matrix. The subsequent local mass loss of 54.81 wt% is caused by intense intra-complex dehydration and destruction of the polymer matrix. The maximum rate of destruction of macromolecular chains is recorded at a temperature of 289.4°C and is ~3.8%/min.

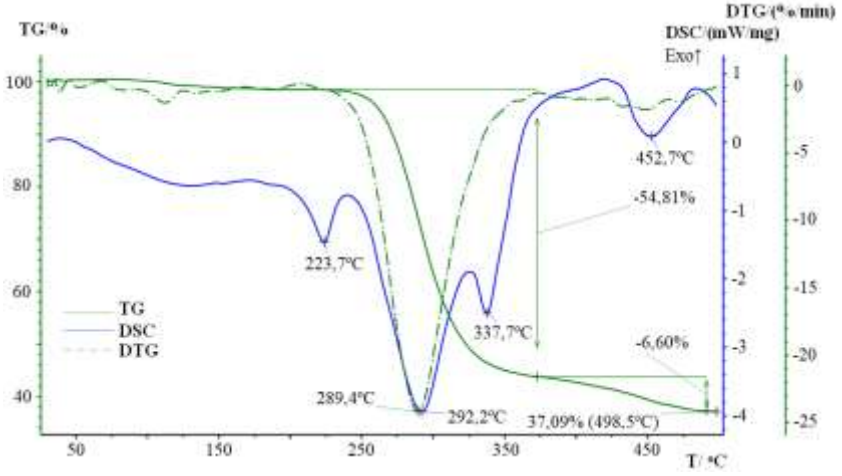


**Fig. 4.** TG, DSC, and DTG patterns of the polymer matrix.

The almost complete coincidence of the DTG maximum with the endothermic peak at 292.2°C on the DSC curve suggests a high synchronicity of thermal and mass transfer processes caused by the destruction of the network of intermolecular hydrogen bonds between the functional groups of matrix components. The intense peak of the degradation rate also indicates a high uniformity of the supramolecular structure and confirms the data on the high segmental compatibility of the matrix components (turbidity spectrum method). The third stage (above 370°C) is characterized by a

slowdown in destructive processes with a loss of 6.60 wt. % and endothermic effect at 452.7°C, corresponding to thermal decomposition and fragmentation of the carbon framework of polymer chains. The residual mass at a temperature of 498.5°C is 37.09% by weight, which confirms the high degree of carbonation of the polymer matrix and indicates the formation of a thermally stable mesh structure.

The spectral profile of the matrix under study (Fig. 5) proves the formation of an extensive system of cooperative hydrogen bonds between macromolecules as a result of cryoconcentration.

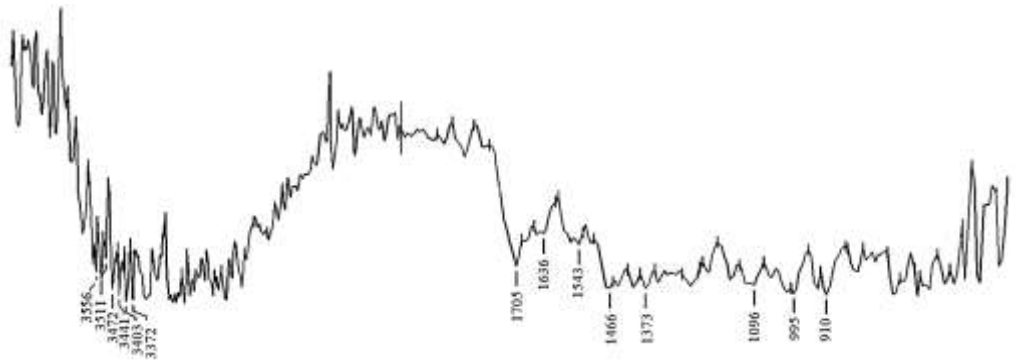


**Fig. 5.** Infrared spectrum of the polymer matrix after cyclic cryogenic structuring.

Cleavage and transformation of the carboxylic region in the range of 1500-1750 $cm^{-1}$ suggests a high degree of completeness of the processes of interpolymer complexation. The absorption band at 1705 $cm^{-1}$ is recorded on the spectrum, due to the valence fluctuations of carbonyl groups (C=O) in the composition of nonionized (free) carboxylic subsystems of polyelectrolyte. However, the key ones are the intense mixed maxima of the absorption bands at 1636 $cm^{-1}$ and 1543 $cm^{-1}$. The peak at 1543 $cm^{-1}$ corresponds to asymmetric valence vibrations of ionized carboxylate anions (COO-), and its intensity indicates the processes of bond polarization and partial proton transfer. This confirms the hypothesis of the formation of strong structures stabilized by intra-complex bonds in interphase cryoconcentrated zones. The absorption band at 1636 $cm^{-1}$ corresponds to the process of involving a significant part of carbonyl groups in the system of intermolecular hydrogen bonds in a trans configuration with OH groups of linear polyol, which confirms the high stability of the formed supramolecular framework and the shift of the main stages of destruction of the carbon skeleton to the region above 200°C (TG/DSC).

The region of 3000-3600 $cm^{-1}$ is characterized by the presence of a multiplet cascade of differentiated absorption bands with maxima at 3556; 3511; 3472; 3441; 3403 and 3372 $cm^{-1}$. The complexity of the multi-peak profile in the region of valence vibrations of OH groups indicates the destruction of the initial intermolecular associates of linear polyol during directional cryostructuring of the matrix. The released OH groups are probably involved in a network of intermolecular contacts with the polyelectrolyte, becoming fixed in the structure of the polymer matrix. This also confirms the data on the high segmental compatibility of the components obtained by the turbidity spectrum method. The discrete nature of the cascade indicates the associated state of residual moisture in the system and explains the low mass loss (0.10 wt. %) at the first low-temperature stage (TG/DSC).

The intense absorption bands at 1466 and 1373 $cm^{-1}$ correspond to the deformation fluctuations of C–H bonds in the methylene and methine groups of macromolecular chains. The high intensity and spectral resolution of the doublet at 1096 and 995 $cm^{-1}$ in combination with the absorption band at 910 cm-1 are due to a change in the conformation of the chains, valence vibrations of C-O bonds and deformation vibrations of OH groups located inside the resulting spatial grid. This confirms that the matrix after cryogenic exposure is a thermodynamically stable, homogeneous system capable of reversible swelling and retaining an excess of active functional groups for effective interaction with the GT surface.

## 3. RESULTS AND DISCUSSION

The resulting composite material is frost-resistant and is characterized by a thermal conductivity of 0.18 W/(m·K). The water resistance index (ti) was at least 3600 s (Russian Standard GOST 12730.5-2018), which corresponds to the maximum brand of water resistance (W20) and indicates the maximum degree of pore coloration by the polymer matrix. The combination of low hydraulic permeability and pronounced thermal insulation properties will ensure a high barrier capacity of the developed composite when used as anti-filtration screens of tailings dumps. High infiltration resistance will reduce the risks of filtration transfer of toxic drainage waters into the environment, and low thermal conductivity will ensure reliable insulation of underlying soils, preventing the degradation of permafrost rocks at the base of hydraulic structures. The mechanism of formation of the composite material structure was studied by powder diffraction, infrared spectroscopy, scanning electron microscopy, and computer X-ray microtomography.

The XRD patterns identifies a series of reflexes confirming the preservation of the BT polymineral framework in the volume of the composite, while a characteristic feature of the profile is the presence of an amorphous halo in the angle range of 2Θ~15-30° (Fig. 6, Table 2). This diffraction effect is associated with X-ray scattering on the disordered spatial grid of the polymer matrix of the composite. The intense reflexes of the BT mineral phases overlap the diffuse scattering region, which confirms the high degree of uniformity of the filler distribution and the absence of macrophase stratification in the system.

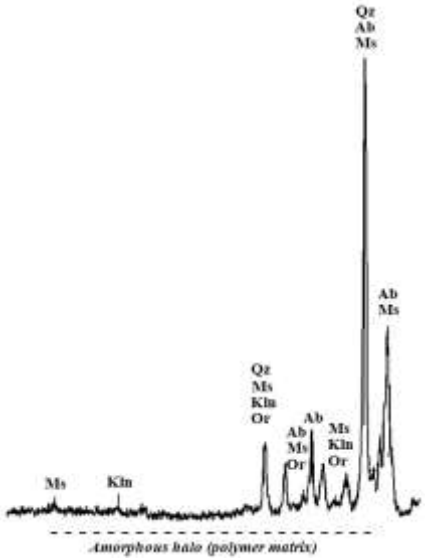


**Fig. 6.** XRD pattern of the composite material.

The main structural markers of the composite are due to the preservation and clear spatial fixation of the basal reflexes of layered hydrosilicates in the low-angle region of muscovite-2M1 (d = 10.27 Å; 2Θ=8.61°) and kaolinite-2M (d = 7.21 Å; 2Θ=12.26°). These diffraction maxima confirm the absence of destruction of the layered structure of hydrosilicates when combining components and indicate the occurrence of interphase processes on the outer contour of mineral particles. In this case, the active centers on the surface of kaolinite and muscovite (≡Al–OH and ≡Si–OH), in combination with metal cations on the highly defective surfaces of GT chips, enter into directed coordination and donor-acceptor interactions with functional groups of matrix components, initiating the formation of polychelate directly at the interface.

**Table 2.** Results of identification of key diffraction maxima and markers of interfacial interaction in the composite.

| 2Θ, (deg.) | *d*, Å | Intensity (cps) | Identified phase and Miller indices (hkl) |
|---|---|---|---|
| 8.61 | 10.27 | 86.5 | Muscovite-2M$_1$ (0,0,2) |
| 12.26 | 7.21 | 112.2 | Kaolinite-2M (0,0,2) |
| 20.67 | 4.29 | 264.0 | Quartz (1,0,0); Muscovite-2M$_1$ (1,1,1); Kaolinite-2M (0,2,1); Orthoclase (2,0,-1) |
| 22.95 | 3.87 | 108.7 | Albite (1,-1,1); Muscovite-2M$_1$ (1,1,-3); Orthoclase (2,0,0) |
| 24.78 | 3.59 | 72.0 | Muscovite-2M$_1$ (1,1,3); Kaolinite-2M (0,0,4); Orthoclase (2,2,-1) |
| 26.48 | 3.36 | 2206.0 | Albite (2,-2,-1); Quartz (0,1,1); Muscovite-2M$_1$, (0,2,4) |

The potassium phase of BT is represented by polymorphic modifications of microcline and saridine, whereas in the diffractogram of the composite (Fig. 6, Table. 2) diffraction maxima of orthoclase are present. The revealed transformation is due to the occurrence of intensive cryogenic and coordination processes at the interface of phases. Significant shear deformations during ore crushing led to the disordering of the surface layers of minerals. Subsequent chemisorption of matrix macromolecules at BT active centers causes relaxation of internal stresses in these defective zones and stabilizes their structure at the phase boundary in the form of a thermodynamically stable modification – orthoclase. The displacement and overlap of the diffraction maxima of potassium spars recorded as polyphase superposition nodes indicates the interphase interaction of the polymer matrix with the alumosilicate BT framework and the formation of polychelate. The presence of a silicate skeleton of the composite is confirmed by the high-intensity superposition reflex of quartz, albite, and muscovite at 2Θ=26.48° (d = 3.36 Å). The characteristic multicentric profile of diffraction lines, which occurs when quartz, kaolinite, albite, and orthoclase maxima overlap, indicates the formation of a developed heterogeneous contact zone. In this area, the macromolecules of the polymer matrix firmly hold BT aggregates due to combined mechanical and chemical interaction.

A comparative analysis of the infrared spectra of the matrix and the filled composite based on it confirms a deep restructuring of the bond system at the supramolecular level (Fig. 7). The process of polychelation in the contact heterogeneous zone is accompanied by a qualitative transformation of the absorption bands of ionized carboxylate anions (COO-). In comparison with the spectrum of the initial matrix (Fig. 5), where the band of symmetric valence vibrations $COO^-$ was fixed at 1543 $cm^{-1}$, its pronounced high-frequency shift to 1559 $cm^{-1}$ is observed in the spectrum of the composite. The recorded shift of the maximum indicates the re-alignment of carboxylate systems and their interaction with metal cations ($Ca^{2+}$, $Mg^{2+}$, $Al^{3+}$), which reached the highly defective surface of BT chips as a result of intensive ore crushing.

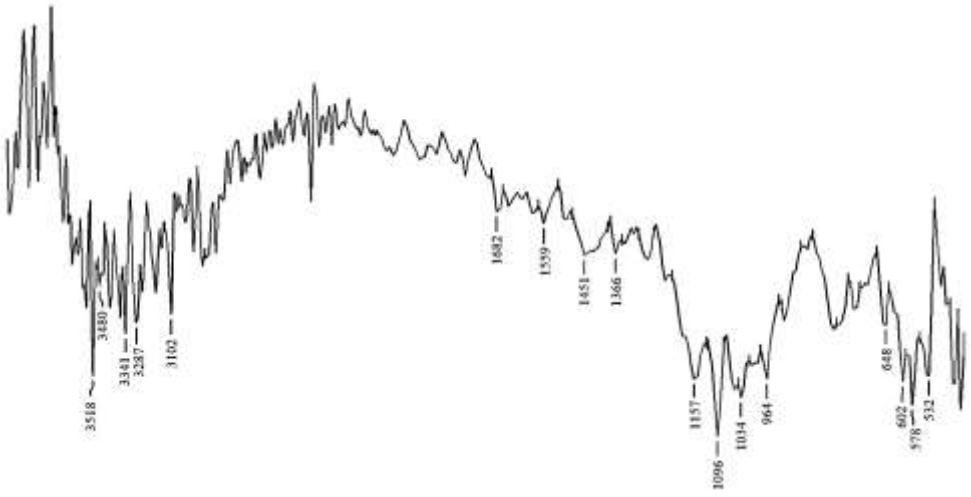


**Fig. 7.** IR-spectra of the composite material.

A decrease in the intensity and a shift in the maximum absorption band of nonionized carbonyl groups (C=O) to 1682 $cm^{-1}$ is recorded, which indicates the low-intensity nature of the residual free carboxyl subsystems and confirms complexation at the interphase boundary. The shifted absorption bands with maxima at 1451 and 1366 $cm^{-1}$ correspond to skeletal deformation vibrations of macromolecular chains (methylene and methine groups). The integration of the BT mineral framework into the volume of the polymer matrix is also confirmed by the restructuring of the spectral profile in the low-frequency region (below 1200 $cm^{-1}$).

The matrix doublet (1096 and 995 $cm^{-1}$) is overlain by an intense wide absorption band of the silicate frame with peaks at 1157, 1096, 1034 and 964 $cm^{-1}$. This spectral cascade is caused by asymmetric valence vibrations of the Si–O–Si and Si–O–Al bonds of the quartz crystal lattice and the formed phase of the orthoclase, which confirms the pore coloration of the formed organomineral system. The overlap and deformation of the absorption bands in the 530-650 $cm^{-1}$ region (648, 602, 578, and 532 $cm^{-1}$), which correspond to valence and deformation vibrations of the Si–O–Al and Al–O interlayer bonds in octahedral layers of muscovite and kaolinite, also indicate the occurrence of chemisorption reactions. The transformation of the profile of the bands of valence vibrations of OH groups (3518, 3480, 3341, 3287, and 3102 $cm^{-1}$) corresponds to the fixation of macromolecular chains of linear polyol and the formation of interphase hydrogen bridges during cryogenic treatment, which also confirms the formation of a defect-free elastic spatial network of interphase coordination engagement.

A comprehensive analysis of a series of micrographs of composite chips obtained on various parts of the surface (Fig. 8a, b, c) made it possible to assess the nature of the spatial distribution of the components, the degree of uniformity of the system, and the morphological features of the interfacial contact. Due to the dependence of the image brightness on the average atomic number of elements (Z-contrast), three main components are revealed in all the studied zones: a dark gray continuous polymer matrix, gray sharp-angled grains of skeleton silicates and quartz, as well as bright white microclusters of iron oxides and sulfide minerals.

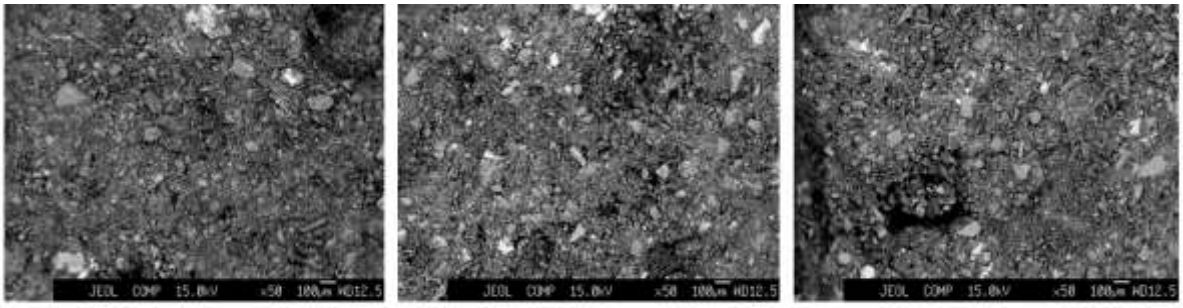


**Fig. 8.** SEM images of composite material (COMP, ×50): a, b – areas of cleavage with a uniform phase distribution; c – zone of macropore localization with an infiltrated polymer structure.

A comparison of the microstructural profile at different cleavage sites (Fig. 8a, b) indicates the formation of a highly filled, homogeneous system with a significant degree of homogeneity of the phase distribution over the entire volume of the material. Highly dispersed BT particles are efficiently distributed in a continuous matrix phase, they fill the interparticle space between larger mineral grains and ensure the formation of a dense polydisperse structure. Figure 8c shows the morphology of the fracture in the area of localization of the macropore (cavity) BT. The defect-free nature of the interfacial boundary in this zone may indicate a high capillary activity of porous macroparticles, which before cryogenic treatment acted as local heterogeneous reservoirs for the initial polymer solution.

Under the influence of capillary pressure, spontaneous infiltration of the inner volume of the cavity probably took place, during which convective transport of highly dispersed particles deep into the pore space of the macrograins took place. Cryogenic treatment contributed to the formation of a stable spatial grid in the volume of the cavity, as well as the colmatation of voids and the fixation of a

monolithic defect-free structure. There are no visible defects, shrinkage voids, or signs of phase separation of mineral grains from the polymer base at the matrix–filler interface. This may indicate high thermodynamic compatibility of the components, strong interfacial adhesion, and indirectly confirm the course of chemisorption reactions and the formation of a polyhelate complex.

The spatial structure of the composite and its geometric parameters in volume were studied by X-ray computed microtomography. Analysis of 777 tomographic sections with a spatial resolution of 15 microns was performed to identify the dependence of the operational properties of the composite (thermal conductivity, frost resistance, water resistance) on its microstructural topology. The parameters of the volume structure of the composite material are given in Table 3.

**Table 3.** Integral and differential parameters of the composite pore network.

| Classification of parameters | Name of the structural parameter, unit of measurement | Meaning |
|---|---|---|
| Volumetric characteristics | Полный исследованный объем, $mm^3$ | 699.77 |
| | The volume of the solid phase, $mm^3$ | 533.78 |
| Integral porosity parameters | Total volumetric porosity, % | 23.72 |
| | Closed (isolated) porosity, % | 0.37 |
| | Open (filtering) porosity, % | 23.44 |
| Topology and geometry of voids | Average size of interstructural distances, μm | 40.47 |
| | Connectivity density of a three-dimensional structure, $mm^{-3}$ | 993.54 |
| Differential distribution of pores (voids) | The proportion of pores 15–45 μm, % | 75.26 |
| | The proportion of pores 45–75 μm, % | 20.62 |
| | The proportion of large pores (caverns) is more than 75 μm, % | 4.12 |

The polymer matrix forms a stable spatial framework (Fig. 9a), which occupies the largest volume of the composite – 76.28% (533.78 $mm^3$). The average thickness of the structural elements was 74.77 μm, and the total porosity index was 23.72%. The proportion of closed pores is only 0.37%, but their extremely high absolute number (167385 units) has been revealed. The ratio of the total volume of closed pores (0.199 $mm^3$) to their number indicates that the average equivalent diameter of one pore is only 13 μm. These pores are distributed in the volume of the polymer framework, forming a highly cellular microstructure with closed air cavities of micron size (Fig. 9b). Cryogenic treatment combined with polychelate crosslinking of the composite components prevented air from merging into large cavities. The presence of micron-sized isolated pores in the material and the absence of macroscopic conditions determine its high water resistance.

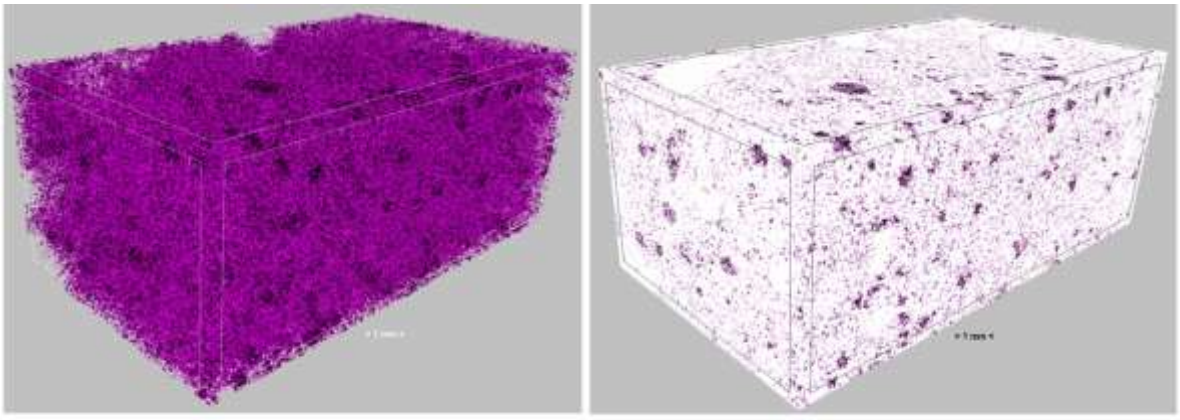


**Fig. 9.** Volumetric microtomographic reconstructions of the spatial structure of a composite material: a – the spatial framework of the polymer matrix (violet phase) and the pore space (black areas); b – the nature of the distribution of closed pores in the volume.

Fig. 10 shows a volumetric reconstruction of the local thicknesses, which makes it possible to determine the nature of the distribution of the elements of the polymer matrix frame. The lintels of the frame (15-45 μm), occupying 10.10% of the volume of the continuous phase, are thin polymer layers at the matrix-filler interface. The supporting frame with a thickness of 45-75 μm accounts for 50.84% of the volume of the continuous phase of the composite, including the matrix and BT (orange-yellow zone). Local zones with a thickness of more than 75 μm account for 39.06% of the volume of the continuous phase (the green-blue zone), where the dominant fraction of 75-105 microns occupies 25.16%. These regions correspond to BT particles and dense coordination nodes of the polychelate crosslinking, acting as supporting elements of the structure.

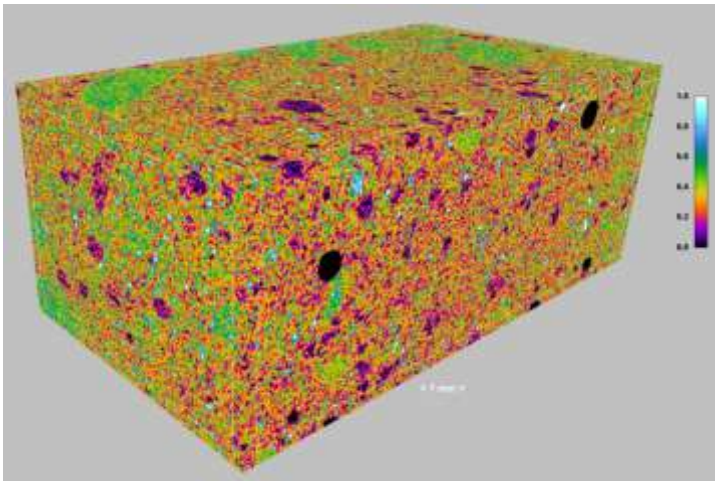

**Fig. 10.** Microtomographic reconstruction of the spatial distribution of the local thickness of the solid phase of the composite material (mm).

A high negative Euler number (-488939) was recorded at a spatial frame connectivity density of 993.54 $mm^{-3}$, which indicates the formation of an elastic branched mesh topology with a significant number of nodes and bridges. This confirms the formation of strong chelate crosslinking nodes between the functional groups of the matrix and metal ions in the BT. The 45-75 μm thick pore walls formed during cryostructuring and the high connectivity of the matrix allow the material to effectively dampen and redistribute internal mechanical stresses that occur when moisture freezes in open channels. The pore space is characterized by a developed sinuous network of small channels (Fig. 11a), which ensures the optimal value of the thermal conductivity of the composite (0.18 W/(m·K)).

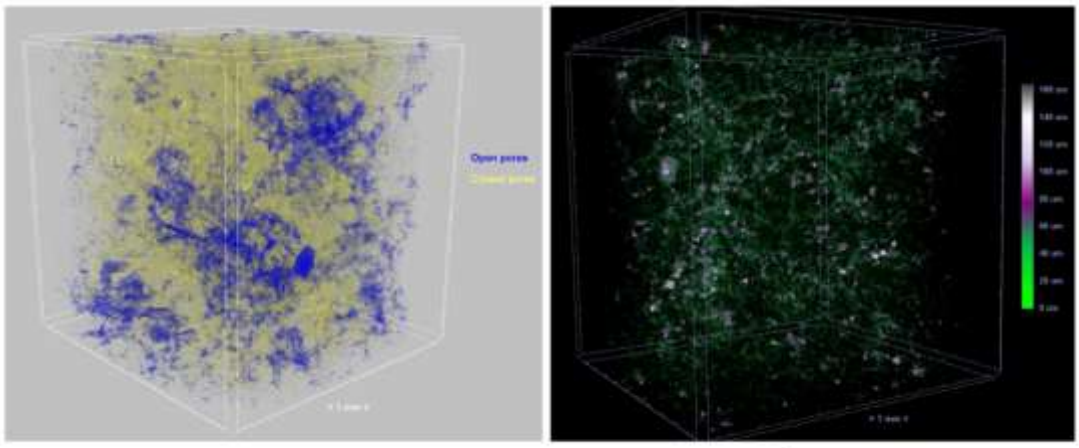

a b

**Fig. 11.** Volumetric microtomographic reconstructions of the elements of the pore structure of a composite material: a – spatial architecture of the channels of the pore network (open pores – blue phase; closed pores – yellow phase); b –pore size distribution (color scale 0-160 μm).

The volumetric model of the pore size distribution (Fig. 11b) shows the regularity of the structure due to the filling of the volume with small pores with sizes of 20-60 μm (green scale). It was found that 75.26% of all voids are micropores with sizes of 15-45 μm. The total proportion of pores up to 75 microns is 95.88%, while channels and caverns larger than 75 μm account for only 4.12% (Table 3).

The analysis of the data obtained in comparison with the parameters of the matrix without filler, the integral porosity of which is 17.1-18.0%, indicates a restructuring of the spatial structure of the material during the introduction of BT and subsequent cryogenic processing. The increase in the total volume porosity of the composite to 23.72% (about 6% relative to the initial matrix) is associated with the physico-chemical interaction of the components of the material. This is manifested in a violation of the continuity of the polymer phase due to the introduction of filler, the appearance of zones of steric confinement of macromolecules at the matrix-filler interface, contributing to the formation of additional interphase micro voids, and the initiation of intensive polychelate binding. The rate of formation of chelate crosslinking nodes probably competes with the rate of compaction of polymer chains during cryogenic processing of the composite, since the fixation of the open microcapillary network is fixed (23.44%). The synergistic effect of the resulting polychelate framework and three cryogenic treatment cycles is to prevent shrinkage of the material with air distribution in the form of ultra-small insulated pores (Fig. 9b), as well as to form a highly connected microcapillary system capable of blocking water filtration.

The effectiveness of chemisorption immobilization of toxic components in the structure of the developed composite is confirmed by the method of biotesting on test objects of two trophic levels *Chlorella vulgaris Beijer* and *Daphnia magna Straus*. The mortality rate of *Daphnia magna Straus* compared with the control was 3.8-7.0%; the deviation in the number of *Chlorella vulgaris Beijer* cells was 1.6-17.4%, which proves the absence of acute toxic effects on test objects. The data obtained convincingly indicate the absence of processes of surface leaching and desorption of toxic components of enrichment tailings in the composition of the composite material.

## 4. CONCLUSIONS

1. The possibility of using waste from the enrichment of gold deposits as a dispersed filler for composite materials with a set of specified properties has been scientifically substantiated. The high reaction potential of the enrichment tailings is due to the presence of feldspar, quartz, and layered hydrosilicates (kaolinite, muscovite) in the composition. The presence of coordination-unsaturated metal cations resulting from ore crushing creates thermodynamically favorable conditions for interfacial polychelation with functional groups of the polymer matrix.

2. The physico-chemical parameters of the polymer matrix determining the homogeneity of the organomineral suspension have been established. It was revealed that partial ionization of carboxylic groups (pH = 6) contributes to the conformational unfolding of polyelectrolyte macrochains and the spatial accessibility of functional groups during interphase polychelation.

3. The mechanism of chemisorption at the matrix-filler interface has been confirmed by infrared spectroscopy and powder X–ray diffraction. The high-frequency shift of the absorption band of asymmetric valence vibrations of ionized carboxylate anions (from 1543 to 1559 $cm^{-1}$) indicates their coordinated binding to metal cations of the filler. Polymorphic transformation of feldspar into orthoclase proves relaxation of internal stresses in defective zones of the heterogeneous contact zone.

4. By the method of computer X-ray microtomography, it was found that the composite material has a continuous spatial frame with an average thickness of 74.77 μm. The connectivity of the spatial polychelate grid is confirmed by the negative value of the Euler number (-488939) at a connectivity density of 993.54 $mm^{-3}$. The dominance of pores with sizes of 15-45 μm (75.26% of the total volume of voids) and the presence of 167385 isolated closed micropores with an average size of 13 μm were revealed.

5. It was found that the low coefficient of thermal conductivity (0.18 W/(m·K)) and the maximum grade of water resistance (W20) of the composite material is determined by the presence of a formed three-dimensional topology of the pore space. Biotesting has experimentally confirmed that the mortality rates of *Daphnia magna Straus* (3.8–7.0%) and the deviation in the number of *Chlorella vulgaris Beijer* cells (1.6–17.4%) are within the normal range. This proves the high efficiency of the

immobilization of toxic components in the structure of the composite material and allows to be recommended for hydro- and thermal insulation of tailings ponds in the cryolithozone.

## 5. ACKNOWLEDGEMENTS

The work was supported by a grant from the Russian Science Foundation (Agreement No. 24-17-20003 dated 04/12/2024) "Scientific substantiation of methods for obtaining composite materials based on waste from the GPC of the Trans-Baikal Territory and the development of technologies for their use in the mining industry"

## REFERENCES

1. Surimbayev B., Bolotova L., Akcil A. et al. Gravity Concentration of Gold-Bearing Ores and Processing of Concentrates: A Review. Mineral Processing and Extractive Metallurgy Review. 2025. 46 (7). P. 726 – 750. https://doi.org/10.1080/08827508.2024.2395824
2. Chingwaru S.J., Tadie M., Von der Heyden B. Characterization of Gold in Complex Historical Refractory Tailings for Enhanced Process Optimization. Mineral Processing and Extractive Metallurgy Review. 2025. 46 (2). P. 193 – 209. https://doi.org/10.1080/08827508.2023.2298728
3. Wu Z., Tao Y., Ran J. et al. Nanobubble-enhanced flotation of auriferous pyrite in gold ore: Behavior and mechanisms. International Journal of Minerals, Metallurgy and Materials. 2025. 32. P. 1826 – 1837. https://doi.org/10.1007/s12613-025-3097-7
4. Erkan E., Ekmekci Z., Altun E. Comparison of flash flotation and gravity separation performance in a greenfield gold project. Physicochemical problems of mineral processing. 2022. 58 (3). P. 146979. https://doi.org/10.37190/ppmp/146979
5. McGrath T.D.H., Staunton W.P., Eksteen J.J. Development of a laboratory test to characterise the behaviour of free gold for use in a combined flash flotation and gravity concentrator model. Minerals Engineering. 2013. 53. P. 276 – 285. https://doi.org/10.1016/j.mineng.2013.08.004
6. Hilger D.M., Blowes D.W., Brookfield A.E. et al. Influence of mine dewatering-effluent cycling on arsenic loading in a gold mine tailings containment area. Water Resources Research. 2025. 61. e2024WR039686. https://doi.org/10.1029/2024WR039686
7. Lemieux J.-M., Frampton A., Fortier P. Recent Advances (2018-2023) and Research Opportunities in the Study of Groundwater in Cold Regions. Permafrost and Periglac Process. 2025. 36. P. 93 – 109. https://doi.org/10.1002/ppp.2255
8. Kallenborn R., Gabrielsen G.W., Vorkamp K. et al. Industrial and public infrastructure as local sources of organic contaminants in the Arctic. Environmental Science: Advances. 2026. 5 (2). P. 304 – 347. https://doi.org/10.1039/d5va00261c
9. He M., Wang L., Yao W. et al. Engineering Applications in Rock Dynamics. In: AI for Rock Dynamics. 2025. Springer, Singapore. https://doi.org/10.1007/978-981-96-5342-3_8
10. Knutsson R., Viklander P., Knutsson S. et al. How to avoid permafrost while depositing tailings in cold climate. Cold Regions Science and Technology. 2018. 153. P. 86 – 96. https://doi.org/10.1016/j.coldregions.2018.05.009
11. Pashkevich M.A., Alekseenko A.V. Reutilization prospects of diamond clay tailings at the Lomonosov mine, Northwestern Russia. Minerals. 2020. 10 (6). P. 517. https://doi.org/10.3390/min10060517
12. Aniskin N.A., Antonov A.S. Numerical Modelling of Tailings Dam Thermal-Seepage Regime Considering Phase Transitions. Modelling and Simulation in Engineering. 2017. 7245413. https://doi.org/10.1155/2017/7245413
13. Edelev A.V., Yurkevich N.V., Gureev V.N. et al. Reclamation of waste storage sites of the mining industry in the Russian Federation. Journal of Mining Science. 2022. 58 (6). P. 1053 – 1068. https://doi.org/10.1134/S1062739122060205

14. Babenko D.A., Pashkevich M.A., Alekseenko A.V. Water quality management at the tailings storage facility of the Gaisky Mining and Processing Plant. Rocznik Ochrona Środowiska. 2020. 22 (1). P. 214 – 225.
15. Fan Y.H., Kerry Rowe R., Brachman R.W.I. et al. Impact of differential settlement on leakage through geomembranes in waste covers. Geosynthetics International. 2025. 32 (1). P. 82 – 93. https://doi.org/10.1680/jgein.23.00175
16. Esford F., Bedell P., Lamontange E. Case study – tailings dam construction in an arctic climate. In Mine Waste 2010: Proceedings of the First International Seminar on the Reduction of Risk in the Management of Tailings and Mine Waste. 2010. P. 181 – 191. https://doi.org/10.36487/ACG_rep/1008_16_Esford
17. Fan J., Rowe R.K. Effect of subgrade on leakage through a defective geomembrane seam below saturated tailings. Geotextiles and Geomembranes. 2023. 51 (2). P. 360 – 369. https://doi.org/10.1016/j.geotexmem.2022.12.003
18. Tuomela A., Ronkanen A.K., Rossi P.M. et al. Using geomembrane liners to reduce seepage through the base of tailings ponds – A review and a framework for design guidelines. Geosciences. 2021. 11(2). P. 93. https://doi.org/10.3390/geosciences11020093
19. Rowe R.K., Fan J. The application of geosynthetics in tailings storage facilities: a general review. Mining. 2024. 4 (2). P. 447 – 468. https://doi.org/10.3390/mining4020026
20. Aparicio-Ardila M.A., Silva J.L.D. Textured high-density polyethylene geomembranes in geotechnical and environmental engineering: an overview. Soils and Rocks. 2026. 49 (2). e2026012325. https://doi.org/10.28927/SR.2026.012325
21. Araujo F.S., Taborda-Llano I., Nunes E.B. et al. Recycling and reuse of mine tailings: A review of advancements and their implications. Geosciences. 2022. 12 (9). P. 319. https://doi.org/10.3390/geosciences12090319
22. Villachica C., Clemente-Jul C., Villachica J. et al. Circular economy in tailings management. Mine Water and the Environment. 2021. 40 (1). P. 23 – 35. https://doi.org/10.1007/s10230-020-00740-4
23. Manaviparast H.R., Miranda T., Pereira E. et al. A comprehensive review on mine tailings as a raw material in the alkali activation process. Applied Sciences. 2024. 14 (12). P. 5127. https://doi.org/10.3390/app14125127
24. Lozinsky V.I., Savina I.N. A study of cryostructuring of polymer systems: 22. Composite poly(vinyl alcohol) cryogels filled with dispersed particles of various degrees of hydrophilicity/hydrophobicity. Colloid Journal. 2002. 64 (3). P. 336 – 343. https://doi.org/10.1023/A:1015920810103
25. Savina I.N., Lozinsky V.I. Study of cryostructuring of polymer systems: 23. Composite poly(vinyl alcohol) cryogels filled with dispersed particles containing ionogenic groups. Colloid Journal. 2004. 66. P. 343 – 350. https://doi.org/10.1023/B:COLL.0000030847.67513.5e
26. Podorozhko E.A., Buzin M.I., Golubev E.K. et al. A study of cryostructuring of polymer systems. 59. Effect of cryogenic treatment of preliminarily deformed poly(vinyl alcohol) cryogels on their physicochemical properties. Colloid Journal. 2021. 83 (5). P. 634 – 641. DOI: 10.1134/S1061933X21050112.
27. Raj N., Selvakumar S., Soundara B. et al. Sustainable utilization of biopolymers as green adhesive in soil improvement: a review. Environmental Science and Pollution Research. 2023. 30 (56). P. 118117 – 118132. https://doi.org/10.1007/s11356-023-30642-1
28. Wiśniewska M., Chibowski S. Influence of temperature and purity of polyacrylic acid on its adsorption and surface structures at the $ZrO_2$/polymer solution interface. Adsorption Science & Technology. 2005. 23 (8). P. 655 – 667. https://doi.org/10.1260/026361705775373279

29. Pankov P., Bespolitov D., Shavanov N. et al. Structural forming of soil composites using as a pavement subgrade strengthening. Case Studies in Construction Materials. 2024. 20. P. e02847. https://doi.org/10.1016/j.cscm.2023.e02847
30. Pankov P., Bespolitov D., Konovalova N. et al. Cryostructuring of Organic-Inorganic Composite Materials Based on Overburden Rocks. Journal of Inorganic and Organometallic Polymers and Materials. 2026. 36. P. 1807 – 1818. https://doi.org/10.1007/s10904-025-03977-0

## INFORMATION ABOUT THE AUTHORS

**Pankov P.P.,** e-mail: zabizht_engineering@mail.ru, ORCID ID: https://orcid.org/0009-0002-7319-0792, SCOPUS: https://www.scopus.com/authid/detail.uri?authorId=57200449338, Transbaikal Institute of Railway Transport, Candidate of Engineering Sciences (Ph.D.), Senior Researcher

**Bespolitov D.V.,** e-mail: zabizht_engineering@mail.ru, ORCID ID: https://orcid.org/0009-0004-8682-6600, SCOPUS: https://www.scopus.com/authid/detail.uri?authorId=57212560482, Transbaikal Institute of Railway Transport, Candidate of Engineering Sciences (Ph.D.), Researcher

**Konovalova N.A.,** e-mail: konovalovanatasha@rambler.ru, ORCID ID: https://orcid.org/0000-0001-7589-9821, SCOPUS: https://www.scopus.com/authid/detail.uri?authorId=57213710725, Transbaikal Institute of Railway Transport, Doctor of Technical Sciences , Professor, Leading Researcher

**Razmakhnin К.К.,** e-mail: zabizht_engineering@mail.ru, ORCID ID: https://orcid.org/0000-0003-2944-7642, SCOPUS: https://www.scopus.com/authid/detail.uri?authorId=56206093000, Transbaikal Institute of Railway Transport, Chita, Russia, Doctor of Technical Sciences (Advanced Doctor), Associate Professor, Senior Researcher

**Shavanov N.D.,** e-mail: zabizht_engineering@mail.ru, ORCID ID: https://orcid.org/0009-0001-6430-2759, SCOPUS: https://www.scopus.com/authid/detail.uri?authorId=58420530500, Transbaikal Institute of Railway Transport, Junior Researcher

**Fediuk R.S.,** roman44@yandex.ru, ORCID ID: https://orcid.org/0000-0002-2279-1240, SCOPUS: https://www.scopus.com/authid/detail.uri?authorId=57199850188, Transbaikal Institute of Railway Transport, Doctor of Technical Sciences (Advanced Doctor), Professor, Leading Researcher